Digital Object Identifier

Wavelet-Based Quantum Sensing of Geomagnetic Fluctuations with Multiple NV Ensembles

CHOU-WEI KIANG[1] and JEAN-FU KIANG [1 2], (LIFE SENIOR, IEEE)
[1]Department of Electrical Engineering, National Taiwan University, Taipei, Taiwan 10617
[2]Graduate Institute of Communication Engineering, National Taiwan University, Taipei, Taiwan 10617
Corresponding author: Jean-Fu Kiang (email: jfkiang@ntu.edu.tw).

ABSTRACT Nitrogen-vacancy (NV) ensembles are viable magnetometers to be implemented on nano-satellites for monitoring geomagnetic fluctuations, which are credible precursors for predicting earthquakes at short notice. In this work, a Haar wavelet-based quantum sensing method is proposed to reconstruct the time-varying waveform of geomagnetic fluctuations in the VLF band. To collect different frequency components of fluctuations waveform at once, we propose a schematic to employ multiple NV ensembles (NVEs), with each controlled by an independent microwave source. Berry sequences are applied on one set of NVEs to extract the scaling coefficients from accumulated geometric phases to reconstruct near-dc components of a waveform. Spin-echo sequences are applied to another set of NVEs to extract the Haar wavelet coefficients from the dynamic phases to reconstruct high-frequency components. The efficacy of the proposed sensing protocol implemented on multiple NVEs is validated by reconstructing a waveform of geomagnetic fluctuations from a DEMETER satellite dataset through simulations. Each NVE is assumed to contain $N = 10^8$ uncorrelated NV centers. The application of a Berry sequence to each NVE can achieve the maximum detectable magnetic field of over $460\ \mu$T, resolving the issues of phase ambiguity and hyperfine-induced detuning if conventional Ramsey sequence were applied. The use of Berry sequences can achieve a sensitivity of ~ 6.8 nT/$\sqrt{\text{Hz}}$, enough for measuring near-dc components of geomagnetic fluctuations in the presence of an ambient geomagnetic field. Spin-echo sequences can achieve a sensitivity of ~ 80 pT/$\sqrt{\text{Hz}}$, enabling faithful reconstruction of high-frequency components in geomagnetic fluctuations. The feasibility of the proposed simulation scenario considering spin-bath noise within an NVE is justified by simulations. The effects of wavelet scales, Rabi frequency in Berry sequence, and number of spins in each NVE are analyzed. The proposed NVE quantum sensors operated with the proposed sensing protocol can be installed on nano-satellites to monitor global geomagnetic fluctuations, with sub-μs temporal resolution in the near future.

INDEX TERMS Quantum sensing, nitrogen-vacancy ensemble (NVE), waveform reconstruction, Haar wavelet, geomagnetic fluctuations, Berry phase, spin echo sequence, spin-bath noise.

I. INTRODUCTION

NEGATIVELY charged nitrogen-vacancy (NV) centers in diamond have been engineered for sensing magnetic and electric fields, mechanical strain, and temperature with high temporal resolution and high sensitivity [1]. Ensemble of NV centers can be used in wide-field microscopic imaging for in-situ studies of electronic, chemical, and biological devices [2], [3]. NV centers were also explored for novel applications in navigation [4], biological electromagnetism at the cellular level [5], and condensed matter physics like probing superconducting vortices and noise currents [6].

Besides their versatile applications, NV centers can tolerate harsh environments with temperatures from cryogenic to 600 K and pressure over 13 GPa [5]. These merits make NV centers and NV ensembles (NVEs) viable as satellite-borne sensors for space explorations.

However, satellite-borne quantum sensors for geomagnetic field measurements were rarely discussed. In [7], the low-frequency geomagnetic-field intensity was detected by using a hybrid technique based on NV-optically detected magnetic resonance (ODMR) and magnetic flux concentrator. However, the idea of using quantum sensors for detecting geomagnetic fluctuations at kHz frequency and sub-nT level was not found in the literature.

The convection currents in the Earth's outer core induce a geomagnetic field of about tens of μT in the ionosphere [8]. Seismic or solar activities may induce geomagnetic fluctuations in the ionosphere and the magnetosphere [9], [10], with a magnitude of sub-nT during a geomagnetically quiet period, and thousands of nT at severe storms [8]. Global distribution of geomagnetic fluctuations in real-time can provide valuable information for studies in seismology, geophysical, and solar activities [11].

Geomagnetic fluctuations are credible earthquake precursors and have been recorded with conventional magnetometers in many events [12]. However, many earthquakes may be missed due to limited coverage of ground-based or airborne magnetometers. On the other hand, satellite-borne sensors can be installed onboard low-earth orbit (LEO) satellites to cover the whole Earth's surface, predicting earthquakes by monitoring geomagnetic anomalies [13].

A. REVIEW ON CONVENTIONAL MAGNETOMETERS FOR EARTH OBSERVATION

In the 21st century, various conventional magnetometers have been deployed on terrestrial satellites for geoscience and remote sensing studies, including geomagnetic field observations [14], [15].

Advanced fluxgate magnetometer (FGM) has been widely adopted in space missions, partly for its relatively low SWaP (size, weight, and power). It can achieve sensitivity below 10 pT/$\sqrt{\text{Hz}}$ and dynamic range over $60,000$ nT [16]. However, FGMs require frequent calibration because their scale factors and voltage offsets change with time and temperature [17].

Helium magnetometer has a fine magnetic field resolution of 5 pT but a narrow operation bandwidth, which can be used as an auxiliary magnetometer for calibrating an FGM [14]. A search-coil magnetometer is inherently sensitive to kHz magnetic fields [12]. Hence, a wide-band magnetometer can be realized by integrating an FGM, for its good near-dc sensitivity, and a search-coil magnetometer [18].

Both proton-precession magnetometers based on nuclear magnetic resonance and optically pumped magnetometers based on electron-spin are endowed with a superior dynamic range of ~ 100 μT, while maintaining sensitivity of ~ 50 pT/$\sqrt{\text{Hz}}$. However, both are bulky in size, consume more than 10 W of power, and weigh several kilograms, constraining their application onboard satellite [17].

Both proton-precession magnetometer and fluxgate magnetometer were installed onboard Ørsted (launched in 1999) and CHAMP (launched in 2000) satellites [15], [19]. Search-coil magnetometer was utilized in DEMETER satellite (launched in 2004) for sensing ac magnetic field [20]. Vector fluxgate magnetometers were installed on satellites of Cryosat-2 (launched in 2010) and Swarm (launched in 2013) [15], [21].

The DEMETER is a micro-satellite launched by CNES for seismo-electromagnetic studies, which was concluded in Dec. 2010 [20]. The electromagnetic signals recorded by the DEMETER satellites have been used to study the ionospheric response to anthropogenic activities and natural phenomena like earthquakes, tsunamis, and volcano eruptions [11]. The waveforms and spectra of magnetic fields in ELF (3 Hz-3 kHz) and VLF (3 kHz-30 kHz) bands were recorded [22] to explore seismo-magnetic phenomena [23], [24] and geomagnetic storms induced by solar winds [25], [26].

A Swarm constellation of low-earth-orbit (LEO) satellites was deployed by the European Space Agency (ESA) and is currently operational at an altitude of 450 km for observing the geomagnetic field [21]. The onboard vector field magnetometer has a wide dynamic range from sub-nT to 65,000 nT, at a sensitivity of a few nT/$\sqrt{\text{Hz}}$ [21]. However, it has a low sampling rate of 50 Hz and its operating temperature is limited between -20 and $40°$C [21].

Energy-efficient nanoscale quantum sensors are promising candidates for magnetometers onboard micro and nano-satellites to measure geomagnetic fields. Examples of these sensors include NV centers, atomic vapor cells, micro-electromechanical systems (MEMSs), and optomechanical magnetometers. Their sensitivity can be further improved by reducing noise and decoherence, possibly via exploiting quantum features like light squeezing and entanglement.

Quantum sensors based on superconducting quantum interference devices (SQUIDs) can achieve sensitivity of sub-fT/$\sqrt{\text{Hz}}$ and a wide operational bandwidth from dc to GHz [27]. A ground-based mobile SQUID magnetometer has been applied for measuring atmospheric noise at extremely low frequency (ELF) and very low frequency (VLF) bands [28]. However, they can only be operated in helium-based cryogenic systems, which are bulky and energy-consuming to go onboard micro/nano-satellites.

B. ADVANTAGES AND POTENTIALS OF NVE MAGNETOMETERS ONBOARD SATELLITES

NVE magnetometers have the merits of operating at room temperature [29], under high pressure and ambient magnetic fields, without resorting to strong bias fields. The nanodiamond host of NV centers is chemically inert and biocompatible, hence can be placed within a few nanometers from a target to achieve spatial resolution of nm in magnetic field imaging [30], [31].

The sensitivity and the signal-to-noise ratio (SNR) of an NVE magnetometer can be improved by a factor of $\sqrt{N_{\text{NV}}}$ if the number of spins in an NVE is increased by N_{NV} folds, assuming the readout signals from individual NV centers are uncorrelated. In [32], an NVE magnetometer embedding $\sim 10^{11}$ NV centers achieved sensitivity of 9 pT/$\sqrt{\text{Hz}}$, by using a 400 mW laser to perform optical initialization and read out. Its sensitivity can be further improved to 400 fT/$\sqrt{\text{Hz}}$ by applying the dynamical decoupling (DD) technique.

In [33], the magnetic field within an NVE magnetometer was enhanced by utilizing a magnetic flux concentrator made of structured magnetic materials to achieve a sensitivity of 0.9 pT/$\sqrt{\text{Hz}}$ in the 10-1000 Hz range, supported with laser power of 200 mW and microwave power of 20 mW. The current sensitivity of NVE magnetometers is close to that of conventional FGMs, and can be further improved. However, the number of photons and hence the required laser power for optical initialization also scale up with the number of NV centers [30]. Considerable power is also consumed for readout and microwave spin control of NVE sensors.

However, high stability and strong environmental resilience of NVE sensors make them viable as next-generation quantum sensors to onboard satellites for measuring geomagnetic fields, space weather, and atmospheric dynamics [34]. A quantum sensing network [35], [36] based on a LEO nano-satellite constellation is envisioned to observe geomagnetic fluctuations globe-wise, achieving time resolution of microseconds and sensitivity of pT/$\sqrt{\text{Hz}}$ [32].

Integrated and portable NVE magnetometers have the merits of economic SWaP design [29], making them promising to be installed on nano-satellites. In 2021, a prototype of portable NVE magnetometers with a sensitivity of 344 pT/$\sqrt{\text{Hz}}$ and a total operational power of ~ 5 W was demonstrated by integrating a single-mode fiber, photodiodes, a 23.5 mW laser module with a size of $35 \times 110 \times 115$ mm^3, a microwave source, and a Helmholtz coil for compensating geomagnetic field [29]. A portable NVE quantum sensor for magnetometry and thermometry of batteries in electric vehicles was proposed in 2021 [37]. It had the size of $35 \times 30 \times 30$ mm^3 and achieved a sensitivity of 3.5 nT/$\sqrt{\text{Hz}}$, supported with a 100 mW laser. In 2022, a portable NVE magnetometer with a size of $4 \times 4 \times 3$ cm^3 was integrated with a 10 mW diode laser and achieved a sensitiviy of 1.43 nT/$\sqrt{\text{Hz}}$ [38]. In short, NVE sensors can be miniaturized to several cm^3 in size, conducive to Earth observation applications based on nano-satellites.

C. PROTOCOLS FOR SENSING MAGNETIC WAVEFORM

Direct Ramsey sensing method is the most straightforward waveform reconstruction method [39], by probing a brief interval of the waveform at a time. The waveform can be directly reconstructed without post-processing. However, this method has limited time resolution and poor sensitivity due to short sensing time.

In [39], a quantum sensing protocol, based on a single NV center, was proposed to restore an arbitrary waveform without post-processing. It achieved a time resolution of 20 ns and a sensitivity of about 4 μT/$\sqrt{\text{Hz}}$. The sensitivity can be further improved to 400 pT/$\sqrt{\text{Hz}}$ by using an NVE containing 10^8 NV centers. However, this approach required the target waveform to repeat at least twice, making it unsuitable for sensing nonrepeatable waveforms of geomagnetic fluctuations.

High temporal resolution is crucial to capture the kHz features in geomagnetic fluctuations. A plausible method is to apply orthogonal bases, such as wavelet functions or Walsh functions, to represent a waveform in terms of a few basis coefficients, which are acquired with multiple quantum sensors in one shot.

Walsh-based method has been used in quantum sensing of time-varying magnetic fields [40]. By utilizing Ramsey sequence and DD sequences, like spin-echo and Carr-Purcell-Meiboom-Gill (CPMG) sequences, different frequency components of a waveform can be encoded in Walsh coefficients. An inverse Walsh transform is then performed to reconstruct the waveform in terms of these Walsh coefficients. Similarly, the Haar wavelet-based method can be implemented by applying Ramsey sequences and spin-echo sequences to derive the coefficients of scaling functions and Haar wavelet functions, respectively.

However, the intrinsic detuning attributed to hyperfine interactions results in phase ambiguity if Ramsey sequences are applied on NVEs, hence the accumulated dynamic phase from readout cannot be mapped to the true magnetic field. In this work, Ramsey sequences are replaced with Berry sequences, to extract the geometric phase and reconstruct near-dc components.

Simulation results of reconstructing magnetic waveform using either Haar or Walsh functions manifest pulse-like artifacts attributed to the pulse-shaped basis functions. Such artifacts can be alleviated by adopting Daubechies wavelets with higher smoothness [41]. The wavelet-based approach proposed in this work can be extended to acquire a more faithful reconstruction of magnetic waveform without inducing pulse-like artifacts.

D. NOVELTIES AND ORGANIZATION OF THIS WORK

Haar wavelet-based quantum sensing was first proposed for detecting nerve impulses [42], and a proof-of-concept experiment was conducted on rescaled signals with magnitudes of a few hundred nT. However, the method in [42] requires signals to have zero dc bias, and the issues of decoherence and dephasing were not elaborated. Inspired by [42], we ameliorate and extend the Haar wavelet method to reconstruct waveforms of geomagnetic fluctuations with magnitude below 0.1 nT in the VLF band while considering the effect of spin-bath noise in an NVE.

In this work, a comprehensive analysis of applying Haar wavelets for quantum sensing magnetic waveform is presented. Theories are derived to explicate the hyperfine-induced detuning and phase ambiguity when applying a Ramsey sequence on an NVE. Berry sequences are proposed in place of Ramsey sequences for extracting the geometric phase, with which to faithfully reconstruct near-dc components of geomagnetic waveforms. A Berry sequence can be realized by adding a continuous, sinusoidal microwave drive between two adjacent pulses in a spin-echo sequence, which compensates for the hyperfine-induced detuning.

The application of NVE quantum sensors for monitoring geomagnetic fluctuations is proposed for the first time, which can benefit researchers in quantum engineering and geoscience research. The efficacy of the proposed approach and deployment scenario are validated by simulations. Several technical challenges are analyzed and overcome.

To extract different frequency components in a waveform of geomagnetic fluctuations in one shot, we propose a novel implementation scheme with multiple NVEs, with each

NVE controlled by an independent microwave drive to yield specific wavelet and scaling coefficients for reconstruction. The time-multiplexing concept is adopted to reuse NVEs whenever possible to reduce the SWaP requirements. Berry sequences are applied on a specific set of NVEs to extract the scaling coefficients for reconstructing near-dc components. Haar wavelet coefficients are extracted by applying spin-echo sequences on another set of NVEs for reconstructing high-frequency components. The efficacy of the proposed sensing protocol is validated by reconstructing a geomagnetic waveform in the VLF band with multiple NVEs. The Lorentzian spin-bath noise model is adopted to simulate spin dephasing. Helmholtz coils are proposed to partially compensate for ambient geomagnetic field, overcoming the dynamic range and sensitivity limitations when applying microwave control sequences on NVEs.

The rest of this work is organized as follows. The simulation framework and scenario are elaborated in Section II, the formulation of waveform reconstruction with NVE sensors is presented in Section III, and the waveform of geomagnetic fluctuations is reconstructed by simulations and analyzed in Section IV. Finally, some conclusions are drawn in Section V.

II. SIMULATION FRAMEWORK AND SCENARIO

A. WAVEFORM REPRESENTATION WITH HAAR WAVELETS AND SCALING FUNCTIONS

The near-dc and high-frequency components of an arbitrary waveform can be represented with the scaling functions and wavelet functions of various scales [43], respectively. The mother Haar wavelet function is defined as [44]

$$\psi\left(\tilde{t}\right)=\begin{cases}1, & 0\le\tilde{t}<1/2\\ -1, & 1/2\le\tilde{t}<1\\ 0, & \text{otherwise}\end{cases}\tag{1}$$

and the corresponding scaling function is defined as [44]

$$\phi\left(\tilde{t}\right)=\begin{cases}1, & 0\le\tilde{t}<1\\ 0, & \text{otherwise}\end{cases}\tag{2}$$

A time-stretching transform $t=T_s\tilde{t}$ is applied to map the mother wavelet in $\tilde{t}\in[0,1]$ to $t\in[0,T_s]$, which is then dilated and translated to form an orthonormal basis $\{h_m^n(t)\}$, where [43], [44]

$$\begin{aligned}h_m^n(t)&=\sqrt{2^m}\psi\left(\frac{2^m}{T_s}t-n\right)\\ &=\begin{cases}2^{m/2}, & \dfrac{nT_s}{2^m}\le t<\dfrac{(n+1/2)T_s}{2^m}\\ -2^{m/2}, & \dfrac{(n+1/2)T_s}{2^m}\le t<\dfrac{(n+1)T_s}{2^m}\\ 0, & \text{otherwise}\end{cases}\end{aligned}\tag{3}$$

is the nth wavelet function in scale m, with $m=0,1,\cdots,M-1$ and $n=0,1,\cdots,2^m-1$. Similarly, the scaling function is time-stretched, dilated, and translated to form another basis $\{\phi_m^n(t)\}$.

An arbitrary magnetic waveform $B_z(t)$ with $t\in[0,T_s]$ can be represented in terms of the Haar wavelet and scaling bases functions as [44]

$$B_z(t)\approx\sum_{\ell=0}^{2^J-1}d_J^\ell\phi_J^\ell(t)+\sum_{m=J}^{M}\sum_{n=0}^{2^m-1}c_m^n h_m^n(t)\tag{4}$$

where J and M are the minimum and maximum wavelet scales, respectively, with $J\le M$,

$$c_m^n=\frac{1}{T_s}\langle B_z,h_m^n\rangle=\frac{1}{T_s}\int_0^{T_s}B_z(t)h_m^n(t)dt\tag{5}$$

is the nth Haar wavelet coefficient of the mth scale, and

$$d_J^\ell=\frac{1}{T_s}\langle B_z,\phi_J^\ell\rangle=\frac{1}{T_s}\int_0^{T_s}B_z(t)\phi_J^\ell(t)dt\tag{6}$$

is the ℓth scaling coefficient of the Jth scale.

The mathematical form of Haar wavelet functions suggests that spin-echo sequences are applied on a set of NVEs to acquire the Haar wavelet coefficients c_m^n, which will be elaborated in Section III-A. Similarly, Berry sequences are applied on another set of NVEs to extract geometric phases, which is related to the scaling coefficients d_J^ℓ. The details will be elaborated in Section III-B.

In addition, the choice of J and M is crucial for reconstructing a waveform. By choosing larger M, more high-frequency components can be acquired to reconstruct a more faithful waveform, at the cost of using more NVEs. The effect of wavelet scales will be analyzed in Section IV-A.

The top inset of Fig.1 shows a sample waveform of geomagnetic fluctuations used in our simulations, which is extracted from the CNES-CDPP database [22] in the VLF band, recorded by the DEMETER satellite, dated 10:51:41.150 UTC on July 1, 2008. The altitude of the DEMETER satellite was 668.6 km, and the ambient geomagnetic field was $\bar{B}_0=(B_{0x},B_{0y},B_{0z})=(0.3072,0.1209,0.2128)$ Gauss. The NV axis is assumed parallel to the z-axis, without loss of generality. The VLF geomagnetic waveform was recorded at a sampling rate of 40 kHz [20], which is interpolated to reach a time resolution of 0.25 μs for simulations. The waveform is segmented into four uniform intervals of $T_s=128$ μs each, with $T_s<T_2$. The waveform in each interval is reconstructed with the proposed method, and then concatenated together to restore the waveform over a longer time span.

B. SAMPLES OF NV ENSEMBLE

In [45], the properties of three NVE diamond samples at room temperature were analyzed. NVEs with longer spin coherence time are desirable to achieve higher sensitivity by applying proper DD sequences or preparing an isotopically pure ^{12}C sample [46]. Hence, it is assumed that each NVE sample in the simulations is isotropically enriched in ^{12}C and contains 10^8 NV centers [47], derived from NV concentration of 10^{14} cm^{-3} [45] and volume of 10^{-3} mm^3. For an

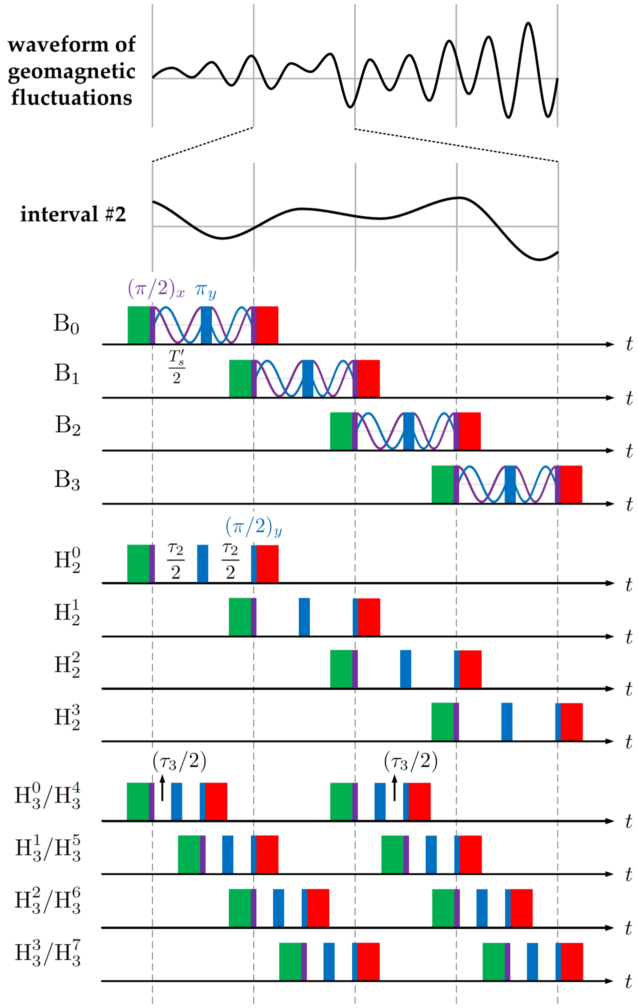

FIGURE 1. The top inset shows a sample waveform of geomagnetic fluctuations with duration $512\ \mu$s, which is segmented into four uniform intervals of length $T_s = 128\ \mu$s each. The waveform in each interval is reconstructed with the proposed quantum sensing protocol. Waveform in interval #2 is reconstructed by applying Berry sequences of $J = 2$ (B_ℓ with $\ell = 0, 1, 2, 3$) to extract scaling coefficients and spin-echo sequences (H_m^n with $m = J, \cdots, M$ and $n = 0, 1, \cdots, 2^m - 1$) to extract Haar wavelet coefficients. Spin-echo sequences with $m = 2, 3$ are illustrated. The envelopes of x and y-polarized microwave drives in Berry sequences are marked purple and blue, respectively. Optical excitation pulses for initialization and readout are marked green and red, respectively.

^{12}C NVE sample with a nitrogen concentration of 1 ppm, the spin-echo coherence time is $T_2 = 240\ \mu$s [45].

A typical measurement process on an NVE sample includes optical initialization, sensing with microwave control, and optical readout. In [47], a measurement on an NVE with $N \sim 10^8$ took an overhead time of $t_o = 900$ ns, including optical initialization pulse duration $t_i = 600$ ns and readout time $t_r = 300$ ns. A delay of $t_d = 6\ \mu$s was required between two consecutive measurements on an NVE to independently acquire the fluorescence signal [47]. These parameters are crucial for designing a time-multiplexing scheme on multiple NVEs.

Table 1 lists the default parameters used in the simulations.

TABLE 1. Default parameters used in simulations.

parameter	symbol	value	ref.
zero-field splitting	$D_{gs}/(2\pi)$	2.87 GHz	[32]
NV spin gyromagnetic ratio	$\gamma_e/(2\pi)$	2.802 MHz/G	[32]
parallel hyperfine parameter	$A_\parallel/(2\pi)$	-2.14 MHz	[48]
transverse hyperfine parameter	$A_\perp/(2\pi)$	-2.70 MHz	[48]
nuclear quadrupole parameter	$P_{gs}/(2\pi)$	-5.01 MHz	[49]
spin-bath coupling strength	Δ	30 kHz	[45]
spin-bath correlation time	τ_c	10 μs	[45]
bias magnetic field	B_s	50 G	[45]
NV centers in each NVE	$N_{\rm NV}$	10^8	[47]
spin-echo decay time	T_2	240 μs	[45]
sensing time per interval	T_s	128 μs	
Berry sensing time	T_s'	16 μs	
minimum Haar-wavelet scale	J	3	
maximum Haar-wavelet scale	M	7	
number of NVEs required	N_e	22	
Rabi frequency	$\Omega_g/(2\pi)$	50 MHz	

A dc magnetic field of $B_s = 50$ G is imposed to distinguish the transitions $|m_s = 0\rangle \leftrightarrow |m_s = +1\rangle$ and $|m_s = 0\rangle \leftrightarrow |m_s = -1\rangle$ in the ground triplet state of an NV center. In this work, an NV qubit is devised to operate on the transition $|m_s = 0\rangle \leftrightarrow |m_s = -1\rangle$.

C. RATIONALES OF USING MULTIPLE NVES AND TIME-MULTIPLEXING SCHEME

The bottom inset of Fig.1 demonstrates the proposed Haar wavelet-based protocol for waveform reconstruction. To reconstruct a nonrepeatable waveform over a finite interval T_s, all the information must be acquired within the same interval.

Fig.1 shows that some of the Berry and spin-echo sequences overlap in operation time windows, implying that some of the wavelet and scaling coefficients cannot be recorded in one shot if only one single NVE is utilized. This issue can be resolved by adopting multiple NVEs which are operated independently to acquire separate coefficients concurrently. To achieve an economic SWaP design, the number of NVEs can be reduced by applying non-overlapping sequences on each of the NVEs via a time-multiplexing scheme that considers overhead time and delay (buffer) time $t_d = 6\ \mu$s between subsequent measurements on each NVE.

Based on the proposed sensing protocol, Fig.2 shows a schematic of an NVE array for reconstructing waveform of geomagnetic fluctuations. A total of N_e NVEs are placed in a two-dimensional array and separated into two groups. Each group is enclosed by a Helmholtz coil to partially compensate for ambient magnetic field to comply with the limits of sensitivity and maximum detectable magnetic field range.

All the NVEs are driven independently with either a Berry sequence or a spin-echo sequence delivered via a coplanar waveguide [37]. The output fluorescence from all the 10^8 NV centers in each NVE is collectively read out with a photodiode [37] and mapped to a specific scaling coefficient or Haar wavelet coefficient for reconstructing the geomagnetic waveform. The scaling coefficients are extracted by applying Berry sequences to designated NVEs in group A, and the wavelet coefficients are extracted by applying spin-echo sequences to designated NVEs in group B.

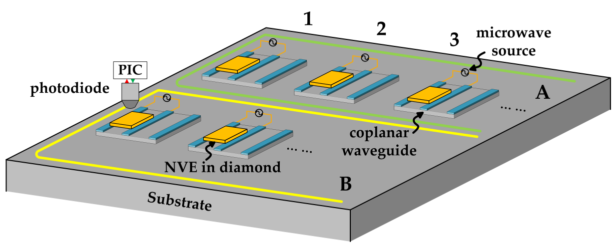

FIGURE 2. Schematic of NVEs for implementing wavelet-based waveform reconstruction of geomagnetic fluctuations. A photonic integrated circuit (PIC) is used to initialize and read out each NVE, with fluorescence signals of each NVE collected by a photodiode. Berry sequences are applied to NVEs in group A (enclosed by green curve) to extract scaling coefficients, and spin-echo sequences are applied to NVEs in group B (enclosed by yellow curve) to extract wavelet coefficients. Two Helmholtz coils carrying adaptive dc currents are used to enclose groups A and B, respectively, to partially compensate ambient geomagnetic field.

Take $J = 3$ and $M = 7$ for example, there are 8 Berry sequences with sensing time $T_s' = 16$ μs. With a total rest time of $t_r = t_o + t_d = 6.9$ μs, two NVEs can be operated alternately to implement these 8 Berry sequences. For instance, NVE #1 in group A shown in Fig.2 can be operated by Berry sequences B_0, B_2, B_4, and B_6, to extract their respective scaling coefficients, while B_1, B_3, B_5, and B_7 can be applied on NVE #2 in group A to extract the other four scaling coefficients.

As for the Haar wavelet of scale $m = 3$, the sensing time for each of the 8 spin-echo sequences is $\tau_3 = 16$ μs, hence two NVEs are needed to extract all these 8 wavelet coefficients. The sensing time for each Haar wavelet of scale $m = 4$ is $\tau_4 = 8$ μs, and two NVEs are needed to extract their wavelet coefficients. Similarly, three, five, and eight NVEs are needed to extract the wavelet coefficients of scales $m = 5$, 6, and 7, respectively. As a result, the total number of NVEs is $N_e = 2+2+2+3+5+8 = 22$ to implement the simulation scenario presented in this work.

D. GENERATION OF SPIN-BATH NOISE WAVEFORM

Several practical factors are considered in the simulations, including the decoherence induced by spin-bath noise and hyperfine interactions between an NV electron spin and neighboring ^{14}N nuclear spins.

The coupling between NV spins and nitrogen spin-bath is characterized by a Lorentzian noise spectrum [45]

$$S(\omega) = \frac{\Delta^2\tau_c}{\pi}\frac{1}{1+(\omega\tau_c)^2} \tag{7}$$

where $\Delta = 30$ kHz is the coupling strength, and $\tau_c = 10$ μs is the correlation time of the spin-bath in a ^{12}C sample. Among the three samples discussed in [45], the ^{12}C sample has the weakest coupling strength between an NV-spin and nitrogen spin-bath due to low ^{13}C nuclear spin impurity and low nitrogen concentration, resulting in a longer coherence of an NVE.

The spin-bath noise is modeled as classical stochastic magnetic field $b_z(t)$ following an Ornstein-Uhlenbeck (O-U) process, with the correlation function [50], [51]

$$C(t,t') = \gamma_e^2\langle b_z(t)b_z(t')\rangle \tag{8}$$

where γ_e is the gyromagnetic ratio of electron spin. Then, the noise spectrum of magnetic field $b_z(t)$ is derived as [52]

$$S(\omega) = \int_{-\infty}^{\infty} C(t'+t,t')e^{i\omega t}dt \ (\mathrm{rad}^2/\mathrm{s}) \tag{9}$$

leading to the Lorentzian spectrum in (7), with the power spectral density (PSD) defined as

$$P(\omega) = \frac{S(\omega)}{\gamma_e^2} \ (\mathrm{T}^2/\mathrm{Hz}) \tag{10}$$

In the simulations, a Python PyCBC toolbox [53] is used to generate $b_z(t)$, a stationary Gaussian noise colored by the Lorentzian noise spectrum in (7), based on the O-U process [54]. An independent noise time series $b_z(t)$ is simulated for each of the 10^8 NV centers in an NVE.

III. FORMULATION OF WAVEFORM RECONSTRUCTION WITH NVE SENSORS

The extraction of Haar wavelet coefficients and scaling coefficients of an arbitrary magnetic waveform is presented in Sections III-A and III-B, respectively. The omission of the transverse magnetic field is justified in Section III-C, and the assumptions behind the proposed method are reverberated in Section III-D.

A. EXTRACTION OF HAAR WAVELET COEFFICIENTS WITH SPIN-ECHO SEQUENCES

Without loss of generality, assume the magnetic field $B_f(t)$ is polarized along the NV axis (z-axis), and the magnetic field of spin-bath noise is $b_z(t)$, then the Hamiltonian of an NV qubit in the lab frame is given by

$$H(t) = \frac{1}{2}\hbar\omega_0\sigma_z + \frac{1}{2}\hbar\gamma_e B_z(t)\sigma_z \tag{11}$$

where

$$B_z(t) = B_f(t) + b_z(t) + 0.001B_{0z} \tag{12}$$

is the effective magnetic waveform sensed by the NV qubit, $\omega_0 = D_{gs} - \gamma_e B_s$ is the Larmor frequency under the dc bias magnetic field B_s for separating $|\pm 1\rangle$ states, D_{gs} is the zero-field splitting of the NV center. We also assume that 99.9% of the ambient geomagnetic field can be compensated for by enclosing the NVEs of group B, as shown in Fig.2, with a Helmholtz coil, yielding the $0.001B_{0z}$ term.

The Hamiltonian of the NV qubit in the rotating frame with Larmor frequency ω_0 is given by

$$H_r(t) = \frac{1}{2}\hbar\gamma_e B_z(t)\sigma_z \tag{13}$$

Thus, an NV qubit evolves under the operator

$$U_{\mathrm{SE}}(t_0,t) = \exp\left\{-\frac{i}{\hbar}\int_{t_0}^{t} H_r(t')dt'\right\} \tag{14}$$

Next, by applying a spin-echo sequence on an NV qubit to modulate the magnetic waveform $B_z(t)$ with the functional form of $h_m^n(t)$ in (3), the accumulated phase is acquired as

$$\varphi_m^n = \gamma_e \left[\int_{n\tau_m}^{(n+1/2)\tau_m} B_z(t)dt - \int_{(n+1/2)\tau_m}^{(n+1)\tau_m} B_z(t)dt \right] \tag{15}$$

which is related to the Haar wavelet coefficient as

$$c_m^n = \frac{1}{T_s}\int_0^{T_s} B_z(t)h_m^n(t)dt = \frac{1}{2^{m/2}\gamma_e T_s}\varphi_m^n \tag{16}$$

The phase φ_m^n is retrieved in the simulations as follows:

1) A $(\pi/2)_x$-pulse is applied to initialize the NV qubit from $|0\rangle$ to the superposition state

$$|\psi_0\rangle = \frac{1}{\sqrt{2}}(|0\rangle - i|1\rangle) \tag{17}$$

2) Then, apply the spin-echo sequence H_m^n on the NV qubit to evolve the state $|\psi_0\rangle$ under operator $U_{\rm SE}\left(\frac{nT_s}{2^m}, \frac{(n+1/2)T_s}{2^m}\right)$ to reach the state

$$|\psi_1\rangle = \frac{1}{\sqrt{2}}e^{-i\varphi_1/2}(|0\rangle - ie^{i\varphi_1}|1\rangle) \tag{18}$$

where

$$\varphi_1 = \gamma_e \int_{n\tau_m}^{(n+1/2)\tau_m} B_z(t)dt \tag{19}$$

3) Apply a π_y-pulse, then the NV qubit evolves freely under operator $U_{\rm SE}\left(\frac{(n+1/2)T_s}{2^m}, \frac{(n+1)T_s}{2^m}\right)$ to reach the state

$$|\psi_3\rangle = \frac{1}{\sqrt{2}}ie^{i\varphi_m^n/2}(|0\rangle - ie^{-i\varphi_m^n}|1\rangle) \tag{20}$$

4) Apply a $(\pi/2)_y$-pulse to reach the state

$$|\psi_f\rangle = \frac{1}{2}ie^{i\varphi_m^n/2}\begin{bmatrix} 1 + ie^{-i\varphi_m^n} \\ 1 - ie^{-i\varphi_m^n} \end{bmatrix} \tag{21}$$

5) Read out the fluorescence and derive the probability of the qubit being at $|0\rangle$ as

$$P_{m,0\to 0}^n = |\langle 0|\psi_f\rangle|^2 = \frac{1}{2}(1 + \sin\varphi_m^n) \tag{22}$$

6) The accumulated phase is estimated as

$$\varphi_m^n = \sin^{-1}(2P_{m,0\to 0}^n - 1) \tag{23}$$

B. EXTRACTION OF SCALING COEFFICIENTS FROM GEOMETRIC PHASE WITH BERRY SEQUENCES

An NV electron spin couples with its neighboring nuclear spins of nitrogen isotopes ^{14}N via hyperfine interactions [55]. Typically, the Ramsey sequence is utilized to capture the near-dc components of a waveform. However, the detuning attributed to hyperfine coupling cannot be refocused with a Ramsey sequence, which does not contain a π-pulse like the spin-echo sequence does [49]. Therefore, we propose to resolve this issue by applying Berry sequences to extract geometric phases instead.

We will first justify why the Ramsey sequence does not work in the presence of the hyperfine-induced detuning. The energy levels of an NV center are barely affected by an external electric field and the nuclear Zeeman effect, as compared to that of an external magnetic field. Thus, the energy levels of an NV center with $S = 1$ can be prescribed with a total Hamiltonian [49], [56], [57]

$$\begin{aligned}\frac{H_{\rm tot}}{\hbar} &\approx D_{gs}S_z^2 + \gamma_e B_s S_z + P_{gs}I_z^2 \\ &+A_\parallel S_z I_z + A_\perp(S_x I_x + S_y I_y)\end{aligned} \tag{24}$$

where $\bar{S}$ is the NV electron spin vector, $(P_{gs}/2\pi) = -5.01$ MHz is the nuclear quadrupole coefficient [49], $\bar{I}$ is the spin vector of ^{14}N nuclear spin [58], $\left(A_\parallel / 2\pi\right) = -2.14$ MHz and $(A_\perp/2\pi) = -2.70$ MHz are hyperfine parameters [48], [59].

The first two terms in the total Hamiltonian imply two resonances at $D_{gs} \pm \gamma_e B_s$, featuring the electron spin transitions of $|m_s = 0\rangle \leftrightarrow |m_s = \pm 1\rangle$, respectively. Note that states $|m_s = 0\rangle$ and $|m_s = -1\rangle$ are selected to form an effective spin-1/2 qubit for quantum sensing.

Next, define a transformation operator $U_r = e^{-i\omega_0 t S_z}$ to derive the Hamiltonian in the rotating frame as

$$\begin{aligned}H_{{\rm tot},r} &= U_r H_{\rm tot} U_r^\dagger + i\hbar\dot{U}_r U_r^\dagger \\ &= \hbar D_{gs}(S_z^2 + S_z) + \hbar P_{gs}I_z^2 + \hbar A_\parallel S_z I_z \\ &+\hbar A_\perp\cos(\omega_0 t)(S_x I_x + S_y I_y) \\ &-\hbar A_\perp\sin(\omega_0 t)(S_x I_y - S_y I_x)\end{aligned} \tag{25}$$

Since D_{gs} falls in the range of GHz, the energy of $|m_s = 1\rangle$ state is very different from those of the other two states, confirming that states $|m_s = 0\rangle$ and $|m_s = -1\rangle$ form an effective qubit.

The energy difference between these two states can be derived from the diagonal elements in (25) as

$$\frac{\Delta H}{\hbar} = P_{gs} + A_\parallel - A_\perp\cos(\omega_0 t) + iA_\perp\sin(\omega_0 t) \tag{26}$$

Thus, the Hamiltonian of the effective spin-1/2 qubit can be approximated as

$$H_r \approx -\frac{\hbar}{2}(P_{gs} + A_\parallel)\sigma_z \tag{27}$$

where $\omega_0 \gg A_\perp$ since ω_0 falls in the range of GHz and $A_\perp$ falls in the range of MHz.

Eqn.(27) suggests that if Ramsey sequences are applied, the hyperfine and quadrupole interaction (in MHz) terms are comparable to an external magnetic field of several hundreds of μT, arousing significant phase ambiguity issue. Thus, a geometric phase magnetometry method [60], [61] is adopted to increase the dynamic range without a significant trade-off in sensitivity. Compared to the quantum phase estimation algorithm commonly adopted to resolve phase ambiguity [62], this method requires less overhead time [60].

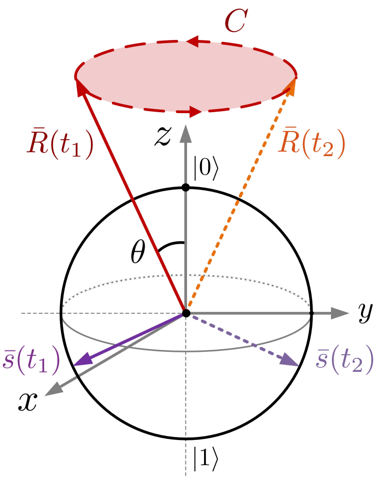

FIGURE 3. Geometric phase accumulation in an NV spin under a Berry sequence. The Bloch vector $\bar{s}(t)$ precesses about a tilted Larmor vector $\bar{R}$(t), which holds a polar angle θ about NV-axis (z-axis) when a microwave drive with Rabi frequency Ω_g is applied on the NV qubit. The geometric phase is accumulated as the trajectory of the Larmor vector tip forms a closed path C.

When a quantum state evolves adiabatically and returns to its initial state, it picks up a geometric phase (Berry's phase) in addition to the dynamic phase [61]. Such geometric phase is independent of time and can be captured by applying a Berry sequence [60].

The Berry sequence is formed by inserting an off-resonant and time-varying continuous microwave sequence between two adjacent pulses of a spin-echo sequence. The spin-echo properties of a Berry sequence make it resilient against the interference of hyperfine and quadrupole couplings, prolonging the coherence time. Meanwhile, the spin-echo properties cancel most of the acquired dynamic phase in a time-varying magnetic field if the magnitude of fluctuations is much smaller than that of dc component within the Berry sensing time T_s', enabling the extraction of scaling coefficients.

Note that even if a Ramsey sequence with deliberately shortened sensing time is applied to measure near-dc components, the detuning attributed to hyperfine and nuclear quadrupole interactions between an NV spin and neighboring nuclear spins still inevitably leads to dynamic phase ambiguity. A geometric phase-based approach is proposed to resolve this issue.

Fig.3 shows a schematic to illustrate the working principle of Berry sequences. During the sensing period of a Berry sequence B_ℓ, a microwave drive with time-dependent polarization along the transverse direction is applied, as shown in Fig.1. The Bloch vector $\bar{s}(t)$ precesses about the Larmor vector $\bar{R}(t)$, under the microwave drive and the external magnetic field $B_z(t)$. The polar angle between the Larmor vector and the z-axis is θ. Meanwhile, the Larmor vector precesses about the z-axis over a complete cycle, with its vector tip moving along the contour C, accumulating a geometric phase in the NV spin.

Although the geometric phase-based method is not affected by hyperfine interactions and increases the maximum detectable magnetic field range, the sensitivity inevitably deteriorates and the power consumption is increased. Hence, we adopt the geometric phase-based approach only to extract the scaling coefficients. The dynamic phase-based approach is kept to extract the wavelet coefficients based on the spin-echo sequences, since the phase ambiguity can be effectively avoided if the ambient geomagnetic field is compensated for with the Helmholtz coil.

During the sensing period of a Berry sequence, the quantum state is governed by an effective Hamiltonian in the rotating frame as [60]

$$H_r(t) = \frac{\hbar}{2}\bar{R}(t)\cdot\bar{\sigma} = H_r^c(t) + H_r^d(t) \tag{28}$$

and the corresponding operator

$$U_B(t_0,t) = \exp\left\{-\frac{i}{\hbar}\int_{t_0}^{t} H_r(t')dt'\right\} \tag{29}$$

where

$$\begin{aligned} H_r^c(t) &= \frac{\hbar\Omega_g}{2}\left\{\cos[\rho(t)]\sigma_x + \sin[\rho(t)]\sigma_y\right\} \\ H_r^d(t) &= \frac{\hbar\gamma_e B_z(t)}{2}\sigma_z \end{aligned} \tag{30}$$

are the control Hamiltonian and the signal Hamiltonian, respectively, Ω_g is the Rabi frequency,

$$\bar{R}(t) = \hat{x}R\sin\theta\cos\rho(t) + \hat{y}R\sin\theta\sin\rho(t) + \hat{z}R\cos\theta \tag{31}$$

is the Larmor vector, $\bar{\sigma} = \sigma_x\hat{x} + \sigma_y\hat{y} + \sigma_z\hat{z}$ is the Pauli matrix, and $\rho(t) = 4\pi t/T_s'$ is the phase of microwave control sequence. From (30), the amplitude of Larmor vector is derived as

$$R = \sqrt{\Omega_g^2 + [\gamma_e B_z(t)]^2} \tag{32}$$

and the polar angle θ is derived as

$$\cos\theta = \frac{\gamma_e B_z(t)}{\Omega_g^2 + [\gamma_e B_z(t)]^2} \tag{33}$$

If the Hamiltonian varies adiabatically, the NV spin qubit will pick up a time-invariant and observable geometric phase after a complete cycle of state evolution. To evaluate the adiabaticity of the NV Hamiltonian, an adiabaticity parameter is defined as [60], [61]

$$A = \frac{d\rho}{dt}\frac{\sin\theta}{2R} = \frac{2\pi\Omega_g}{T_s'[\Omega_g^2 + [\gamma_e B_z(t)]^2]} \approx \frac{2\pi}{T_s'\Omega_g} \tag{34}$$

In the adiabatic regime where $A \ll 1$, the Larmor vector tip forms a closed contour C on the Bloch sphere. In [61], the difference between the measured geometric phase and the Berry phase is negligible under $A \leq 0.04$.

Assuming that the Larmor vector rotation is adiabatic, the two instantaneous eigenstates are derived from the Hamiltonian in (28) as

$$\begin{aligned} |E_+^{\bar{\alpha}}\rangle &= \cos\frac{\theta}{2}|0\rangle + e^{i\rho}\sin\frac{\theta}{2}|1\rangle \\ |E_-^{\bar{\alpha}}\rangle &= -\sin\frac{\theta}{2}|0\rangle + e^{i\rho}\cos\frac{\theta}{2}|1\rangle \end{aligned} \tag{35}$$

Then, the corresponding Berry connections are defined as

$$\bar{A}_{\pm}(\bar{\alpha}) = i\langle E_{\pm}^{\bar{\alpha}}|\nabla_{\bar{\alpha}}|E_{\pm}^{\bar{\alpha}}\rangle = \hat{\phi}i\frac{1\mp\cos\theta}{2r\sin\theta} \tag{36}$$

which yields the geometric phase

$$\varphi^g = \oint_C \bar{A}_{\pm}(\alpha)\cdot d\bar{\alpha} = \mp\frac{\Theta}{2} \tag{37}$$

accumulated in the ground and excited states, respectively, where C is the closed contour shown in Fig.3, $\Theta = 2\pi(1-\cos\theta)$ is the solid angle subtended by C at the origin, $\bar{\alpha} = \hat{r}R + \hat{\theta}\theta + \hat{\phi}\rho$, and

$$\nabla_{\bar{\alpha}} = \hat{\theta}\frac{1}{r}\frac{\partial}{\partial\theta} + \hat{\phi}\frac{1}{r\sin\theta}\frac{\partial}{\partial\rho} \tag{38}$$

is the gradient with respect to $\bar{\alpha}$, under an approximately constant R.

By exerting a Berry sequence B_ℓ, as demonstrated in Fig.1, the accumulated geometric phase in the NV qubit is extracted to determine the scaling coefficient as follows:

1) Apply a $(\pi/2)_x$-pulse to initialize the state as

$$|\psi_0\rangle = \frac{1}{\sqrt{2}}(|0\rangle - i|1\rangle) \tag{39}$$

2) The NV qubit evolves under operator $U_B(\ell T_s', (\ell+1/2)T_s')$ to reach the state

$$|\psi_1\rangle = \frac{1}{\sqrt{2}}(e^{-i(\varphi_\ell^d+\varphi_\ell^g)/2}|0\rangle - ie^{i(\varphi_\ell^{d1}+\varphi_\ell^{g1})/2}|1\rangle) \tag{40}$$

where

$$\varphi_\ell^{d1} = \gamma_e\int_{\ell T_s'}^{(\ell+1/2)T_s'} B_z(t)dt \tag{41}$$

$$\varphi_\ell^{g1} = \Theta \tag{42}$$

are the relative dynamic and geometric phases, respectively, accumulated during the first half of the sequence.

3) Apply a π_y-pulse to invert the qubit state as $|\psi_2\rangle$.

4) The NV qubit evolves under the operator $U_B((\ell+1/2)T_s', (\ell+1)T_s')$, with $\rho(t)$ in the Hamiltonian of (28) replaced with $-\rho(t)$ to reverse the polarization of the microwave drive in the control Hamiltonian $H_r^c(t)$. Hence, the rotation direction of the Larmor vector is reversed, the accumulated geometric phase is effectively doubled after applying the Berry sequence, and the state evolves to

$$\begin{aligned}|\psi_3\rangle &= \frac{1}{\sqrt{2}}\left[ie^{i(\varphi_\ell^{d1}-\varphi_\ell^{d2}+\varphi_\ell^{g1}-\varphi_\ell^{g2})/2})|0\rangle\right.\\ &\qquad \left.+e^{-i(\varphi_\ell^{d1}-\varphi_\ell^{d2}+\varphi_\ell^{g1}-\varphi_\ell^{g2})/2}|1\rangle\right]\\ &\approx \frac{1}{\sqrt{2}}\left[ie^{i\Theta}|0\rangle + e^{-i\Theta}|1\rangle\right]\end{aligned} \tag{43}$$

where

$$\varphi_\ell^{d2} = \gamma_e\int_{(\ell+1/2)T_s'}^{(\ell+1)T_s'} B_z(t)dt \approx \varphi_\ell^{d1} \tag{44}$$

$$\varphi_\ell^{g2} = -\Theta = -\varphi_\ell^{g1} \tag{45}$$

are the relative dynamic and geometric phases, respectively, accumulated in the second half of the sequence. It is assumed that the geomagnetic field $B_z(t)$ fluctuates within a small range such that the dynamic phase in the quantum state cancels out during the spin-echo sequence, leaving only the geometric phase in the readout of the NV qubit.

5) Apply a $(\pi/2)_x$-pulse to reach the state

$$|\psi_f\rangle = \frac{1}{2}ie^{i\Theta}\begin{bmatrix}1-e^{-i2\Theta}\\ -i(1+e^{-i2\Theta})\end{bmatrix} \tag{46}$$

6) Read out the fluorescence and derive the probability of the qubit being at $|0\rangle$ as

$$P_{\ell,0\to 0}^g = |\langle 0|\psi_f\rangle|^2 = \frac{1}{2}[1-\cos(2\Theta)] \tag{47}$$

7) The accumulated geometric phase is estimated as

$$\varphi_\ell^g = \cos^{-1}(1-2P_{\ell,0\to 0}^g) + 2N\pi = 2\Theta \tag{48}$$

where N is properly chosen to unwrap the phase. The acquired geometric phase is used to determine the corresponding scaling coefficient as

$$\varphi_\ell^g = 2\Theta = 4\pi\left(1-\frac{\gamma_e d_J^\ell}{\sqrt{(\gamma_e d_J^\ell)^2+\Omega_g^2}}\right)$$

leading to

$$d_J^\ell = \frac{\Omega_g}{\gamma_e}\left[\left(1-\frac{\varphi_\ell^g}{4\pi}\right)^{-2}-1\right]^{-1/2} \tag{49}$$

Finally, we elaborate the reason to keep a fraction of ambient geomagnetic field B_{0z} to comply with the Berry sensitivity limit. If the external magnetic field B_z remains constant within the sensing time T_s', its dynamic phase can be fully compensated for with a Berry sequence bearing the spin-echo nature. However, since $B_z(t)$ is time varying, the associated dynamic phase cannot be entirely eliminated, and the residual dynamic phase increases with the magnitude of $B_z(t)$. If the entire ambient magnetic field B_{0z} is kept in $B_z(t)$, undesirable distortion will occur in the reconstructed waveform due to the residual dynamic phase. On the other hand, if B_{0z} is entirely compensated for with a Helmholtz coil, the resulting $B_z(t)$ will fall below the Berry sensitivity level, resulting in erroneous reconstruction.

Hence, we propose a Helmholtz coil to enclose the NVEs of group A, as shown in Fig.2, to compensate for 95% of the ambient geomagnetic field, reducing the effective magnetic waveform in (30) to

$$B_z(t) = B_f(t) + b_z(t) + 0.05B_{0z} \tag{50}$$

The residual 5% of ambient magnetic field guarantees that $B_z(t)$ is at least on the order of $\sim 1\ \mu$T, falling within the dynamic range and well above the sensitivity limit. Meanwhile, the waveform will not be distorted because the accumulated dynamic phase is mostly canceled.

C. EFFECTS OF TRANSVERSE MAGNETIC FIELD

In this Subsection, we will prove that the magnetic field transverse to the NV spin can be neglected. Consider a system composed of an NV center and a ^{14}N nuclear spin, in the presence of a vector geomagnetic field $\bar{B}(t) = \hat{x}B_x(t) + \hat{y}B_y(t) + \hat{z}B_z(t)$, the Hamiltonian in the rotating frame is

$$\begin{aligned}
H_{\text{tot},r} = &\hbar D_{gs}\left(S_z^2 + S_z\right) + \hbar P_{gs} I_z^2 \\
&+\hbar A_{\|} S_z I_z + \hbar\gamma_e B_z(t) S_z \\
&+\hbar A_{\perp}\cos(\omega_0 t)(S_x I_x + S_y I_y) \\
&-\hbar A_{\perp}\sin(\omega_0 t)(S_x I_y - S_y I_x) \\
&+\hbar\gamma_e\left[B_x(t)\cos(\omega_0 t) - B_y(t)\sin(\omega_0 t)\right] S_x \\
&+\hbar\gamma_e\left[B_x(t)\sin(\omega_0 t) + B_y(t)\cos(\omega_0 t)\right] S_y
\end{aligned} \tag{51}$$

Next, apply a second-order perturbation theory to evaluate the impact of a transverse magnetic field on the energy levels. The first term on the right-hand side of (51) falls in the range of GHz, while the other terms fall in the range of MHz or lower. Thus, the Hamiltonian in (51) can be approximated as

$$H_{\text{tot},r} = H_{0r} + \epsilon H_{1r} \tag{52}$$

with the dominant term of $H_{0r} = \hbar D_{gs}\left(S_z^2 + S_z\right)$ and the perturbation term of ϵH_{1r}. By applying the perturbation theory, the energy difference between $|m_s = 0\rangle$ and $|m_s = -1\rangle$ states is derived to the second-order as

$$\Delta\tilde{\omega}_- \approx P_{gs} + A_{\|} - \gamma_e B_z(t) + \frac{\gamma_e^2\left[B_x^2(t) + B_y^2(t)\right]}{P_{gs} + A_{\|} - \gamma_e B_z(t)} \tag{53}$$

where the sinusoidal terms are neglected since $\omega_0 \gg A_{\perp}$.

Given the ambient geomagnetic field $\bar{B}_0$ mentioned in Section II-A, the second-order term in (53) is estimated as 0.1105 MHz, which is $\sim$ 70 times smaller than the other terms combined. Hence, it is reasonable to neglect the effect of the transverse magnetic field in our simulations.

In summary, the magnetic field component aligned with the NV axis can be reconstructed without being perturbed by the transverse magnetic field components. This implies that a vector geomagnetic waveform can be reconstructed by using NVEs with NV centers aligned in different crystallographic axes of diamond lattice, and these NV centers are not affected by the transverse field components with respect to their own NV spin axes.

D. RECONSTRUCTION OF GEOMAGNETIC WAVEFORM

Ideally, a single NV qubit can be used to reconstruct the geomagnetic waveform in the absence of noise. In practice, it is very challenging to extract wavelet and scaling coefficients by exciting and reading out a single NV qubit in an NVE sample of diamond, especially when the spin-bath noise is much stronger than the weak geomagnetic fluctuations.

The schematic in Fig.2 contains N_e NVEs, with each NVE embedding $N_{\rm NV}$ NV qubits. We assume that each NV qubit senses the same geomagnetic fluctuations under spin-bath noise independent from the other NV qubits.

As illustrated in Section II, an NVE is operated with a specific Berry or spin-echo sequence to extract the corresponding scaling or wavelet coefficient. If NVE #1 of group A is driven by a Berry sequence B_0 of sensing time $T_s' = 16$ μs to extract a scaling coefficient d_3^0, the ensemble average of transition probability is estimated as

$$\langle P_{0,0\to 0}^g\rangle = \frac{1}{N_{\rm NV}}\sum_{p=1}^{N_{\rm NV}} P_{0p,0\to 0} \tag{54}$$

which can be generalized to $P_{\ell p,0\to 0}^g$ for the pth NV qubit under the ℓth Berry sequence, with definition similar to (47).

Similarly, if NVE #1 of group B is driven by a spin-echo sequence H_3^0 of sensing time $\tau_3 = 16$ μs to extract a Haar wavelet coefficient c_3^0, the ensemble average of transition probability is estimated as

$$\langle P_{3,0\to 0}^0\rangle = \frac{1}{N_{\rm NV}}\sum_{p=1}^{N_{\rm NV}} P_{3p,0\to 0}^0 \tag{55}$$

which can be generalized to $P_{mp,0\to 0}^n$ for the pth NV qubit under the nth spin-echo sequence of the mth scale, with definition similar to (22).

From the ensemble average of transition probabilities, the Haar wavelet and scaling coefficients contributed by the geomagnetic fluctuations are estimated as

$$\tilde{c}_m^n = \frac{1}{2^{m/2}\gamma_e T_s}\sin^{-1}(2\langle P_{m,0\to 0}^n\rangle - 1) \tag{56}$$

$$\tilde{d}_J^\ell = \frac{\Omega_g}{\gamma_e}\left[\left(1 - \frac{\sin^{-1}(1 - 2\langle P_{\ell,0\to 0}^g\rangle) + 2N\pi}{4\pi}\right)^{-2} - 1\right]^{-1/2} \tag{57}$$

which are substituted into the inverse wavelet transform to yield the reconstructed geomagnetic waveform as

$$\begin{aligned}
\tilde{B}_z(t) &= \sum_{\ell=0}^{2^J-1}\tilde{d}_J^\ell\phi_J^\ell(t) + \sum_{m=J}^{M}\sum_{n=0}^{2^m-1}\tilde{c}_m^n h_m^n(t) \\
&\approx \tilde{B}_f(t) + 0.05B_{0z}
\end{aligned} \tag{58}$$

where the noise effects are mitigated by taking the ensemble average over $N_{\rm NV} = 10^8$ NV qubits in each NVE, revealing the information pertinent to geomagnetic fluctuations, and the $0.05B_{0z}$ term is the 5% of ambient geomagnetic field in (50). By subtracting $0.05B_{0z}$ from $\tilde{B}_z(t)$, the waveform of geomagnetic fluctuations, $\tilde{B}_f(t)$, is reconstructed. Note that a residual ambient field of $0.001B_{0z}$ is considered in Section III-A, but the wavelet functions tend to filter out near-dc components in the extraction of wavelet coefficients.

IV. SIMULATIONS AND DISCUSSIONS

A. EFFECTS OF WAVELET SCALES

Given a minimum scale J, the choice of maximum scale M involves a trade-off between the required resources and the reconstruction error. If M is too small, the high-frequency components cannot be fully restored. On the other hand, reconstruction error is reduced with larger M, at the cost of using more NVEs.

The optimal value of wavelet scales can be determined by comparing the reconstruction fidelity of geomagnetic fluctuation waveform under various combinations of J and M. To evaluate the deviation between the true waveform $B_f(t)$ and the reconstructed waveform $\tilde{B}_f(t)$, a normalized root mean square error (NRMSE) is defined as

$$\mathrm{NRMSE}\left(B_f,\tilde{B}_f\right)=\sqrt{\frac{\displaystyle\int_0^{T_s}\left|\tilde{B}_f(t)-B_f(t)\right|^2 dt}{\displaystyle\int_0^{T_s}\left|B_f(t)\right|^2 dt}} \quad (59)$$

TABLE 2. NRMSE of reconstructing geomagnetic fluctuations waveform under various combinations of J and M, with $A=0.00125$. The Berry sensing intervals are $T_s'=128, 32, 16, 8$ μs for $J=0,2,3,4$, respectively.

J	M	NRMSE ($\times 10^{-6}$)	J	M	NRMSE ($\times 10^{-6}$)
0	2	39.984	3	4	11.764
0	4	21.522	3	6	7.563
0	6	19.547	**3**	**7**	**7.294**
0	8	19.416	3	8	7.218
0	10	19.406	3	10	7.197
2	2	44.201	4	4	39.385
2	4	28.604	4	6	38.341
2	6	27.150	4	7	38.288
2	8	27.055	4	8	38.274
2	10	27.050	4	10	38.270

Fig.4 shows the proof-of-concept simulation on reconstructing the waveform in Fig.1, assuming the NVEs are placed in a noiseless environment. Table 2 indicates that if J is fixed, the NRMSE decreases as M is increased and saturates at $M=6$, which is related to the spectrum of the target geomagnetic waveform in Fig.1.

Fig.4(a) manifests obvious pulsed-shape defects with $J=3$ and $M=4$, suggesting that $M>4$ is required. The reconstructed waveforms with $M=7$ and $M=10$ are very similar, suggesting that most of the high-frequency components have already been captured with $M=7$.

On the other hand, Table 2 reveals no obvious trend in NRMSE versus J. For waveforms with different spectra, the optimal value of J can be varied to faithfully reconstruct the near-dc components and minimize the difference of dynamic phases acquired between the first and the second halves of a Berry sensing period.

Fig.4(b) shows the reconstructed waveforms with a fixed $M=7$ and various J. It is observed that the reconstructed waveform with $J=3$ matches the best with the target waveform, which is confirmed with Table 2 that the NRMSE is minimized by choosing $J=3$. Hence, $J=3$ and $M=7$ are adopted in the subsequent simulations.

B. SENSITIVITY ANALYSIS

Field experiments indicate that shot noise, laser power noise, and electronic noise can deteriorate the sensitivity of an NV magnetometer [38]. The laser noise can be reduced by adopting a common-mode rejection method [63], and the electronic noise can be alleviated by utilizing high-quality microwave sources and modulating the signal with lock-in amplifiers to achieve system noise below 100 pT/$\sqrt{\mathrm{Hz}}$ [38]. In this Subsection, the photon-shot-noise-limited sensitivity of spin-echo sequences and Berry sequences will be analyzed under readout fidelity $\mathcal{F}\ll 1$, assuming that laser noise and electronic noise are minimized.

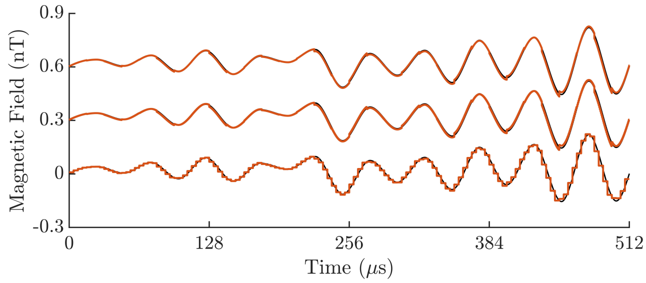

(a)

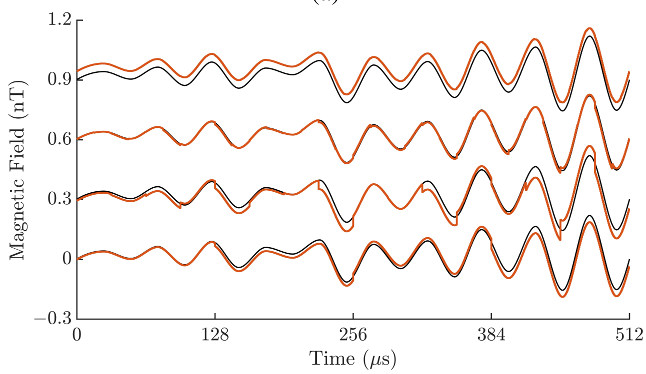

(b)

FIGURE 4. Reconstruction of geomagnetic fluctuations waveform with wavelet scales (J, M) in a noiseless environment, $N_{\mathrm{NV}}=1$, ———: waveform in Fig.1, ———: reconstructed waveform. (a) $J=3$, $M=4,7,10$ from bottom to top, (b) $M=7$, $J=0,2,3,4$ from bottom to top. The curves are offset by 0.3 nT for clarity.

1) Spin-Echo Sequence

The photon-shot-noise-limited sensitivity of applying a spin-echo sequence on an NVE is defined as [30]

$$\begin{aligned}\eta_{\mathrm{SE}}^{\mathrm{psn}} &\approx \frac{\pi}{2}\frac{1}{\gamma_e}\frac{1}{\mathcal{F}e^{-(\tau_m/T_2)^p}\sqrt{N_{\mathrm{NV}}}}\frac{\sqrt{t_I+\tau_m+t_R}}{\tau_m}\\ &=82.41\frac{\mathrm{pT}}{\sqrt{\mathrm{Hz}}}\end{aligned} \quad (60)$$

where $T_2=240$ μs [45], $p\simeq 1.5$ for ^{12}C NVE sample [64], the optical initialization pulse width is $t_I=600$ ns, the readout laser pulse width is $t_R=300$ ns, and the fidelity is $\mathcal{F}=1/67$ [47]. The shortest spin-echo sensing time is $\tau_7=1$ μs with the maximum Haar wavelet scale $M=7$. The sensitivity can be further improved by increasing τ_m or utilizing NVE samples with larger N_{NV}.

2) Berry Sequence

Similarly, the hoton-shot-noise-limited sensitivity of applying a Berry sequence on an NVE is defined as [30], [60]

$$\eta_{\text{Berry}}^{\text{psn}} \approx \frac{\pi}{2} \frac{\sqrt{T_s'}}{dP_\ell^g/dd_J^\ell\big|_{\max}} \frac{1}{\mathcal{F}e^{-(T_s'/T_2)^p}\sqrt{N_{\text{NV}}}} \sqrt{\frac{t_I + T_s' + t_R}{T_s'}}$$
$$= \frac{\pi}{4A}\frac{1}{\gamma_e}\frac{1}{\mathcal{F}e^{-(T_s'/T_2)^p}\sqrt{N_{\text{NV}}}} \frac{\sqrt{t_I + T_s' + t_R}}{T_s'} \quad (61)$$

where A is the adiabaticity parameter and the maximum slope of population difference between two quantum states after readout is derived as

$$\left.\frac{dP_\ell^g}{dd_J^\ell}\right|_{\max} \approx \frac{4\pi\gamma_e}{\Omega_g} = 2A\gamma_e T_s' \quad (62)$$

In the subsequent simulations, we choose $T_s' = 16$ μs with $J = 3$, based on the analysis in Section IV-A. The Rabi frequency is chosen as $\Omega_g/(2\pi) = 50$ MHz, leading to an adiabaticity of $A = 2\pi/(\Omega_g T_s') = 0.00125$, which will be derived in Section IV-C. Hence, the sensitivity is estimated with (61) as

$$\eta_{\text{Berry}}^{\text{psn}} \approx 6.789 \frac{\text{nT}}{\sqrt{\text{Hz}}} \quad (63)$$

C. EFFECTS OF RABI FREQUENCY AND RESERVED AMBIENT MAGNETIC FIELD

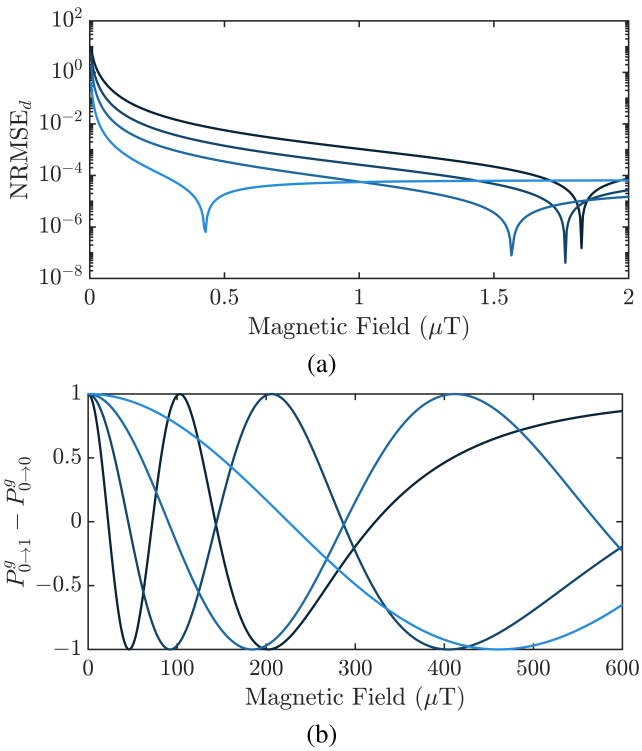

FIGURE 5. (a) NRMSE$_d$ between simulated scaling coefficient $\tilde{d}_J^\ell$ and theoretical scaling coefficient d_J^ℓ over a small range of B_z. (b) Readout probability difference $(P_{0\to1}^g - P_{0\to0}^g)$ over a wider range of B_z. The four curves colored from dark blue (———) to light blue (———) are associated with $\Omega_g/(2\pi) = 5, 10, 20, 50$ MHz, respectively.

TABLE 3. Effects of Ω_g on NRMSE, sensitivity, and maximum detectable magnetic field of Berry sequences, with $N_{\text{NV}} = 1$, $J = 3$, $M = 7$, $T_s' = 16$ μs.

$\Omega_g/(2\pi)$ (MHz)	A	NRMSE	$\eta_{\text{Berry}}^{\text{psn}}$ (nT/$\sqrt{\text{Hz}}$)	$B_{\text{Berry}}^{\max}$ (μT)
5	0.01250	8.943×10^{-4}	0.6789	46.066
10	0.00625	2.165×10^{-4}	1.3577	92.132
20	0.00313	4.682×10^{-5}	2.7155	184.264
50	0.00125	$\mathbf{7.290 \times 10^{-6}}$	6.7886	460.659

The adiabaticity defined in (34) is affected by the Berry sensing time T_s' and the Rabi frequency Ω_g. Next, proof-of-concept simulations are conducted to evaluate the effects of Ω_g on waveform reconstruction in terms of NRMSE, sensitivity, and maximum detectable magnetic field, with $N_{\text{NV}} = 1$ and $T_s' = 16$ μs.

Table 3 shows that the adiabaticity A decreases monotonically as the Rabi frequency Ω_g is increased. Also, the NRMSE decreases monotonically with increaing Rabi frequency, implying a more accurate waveform reconstruction, which can be attributed to the nonlinear mapping between the accumulated geometric phase φ_ℓ^g and the scaling coefficient d_J^ℓ in (49). This nonlinear mapping leads to a deviation between the simulated and theoretical relation of φ_ℓ^g-d_J^ℓ in the small-field regime.

To quantify this deviation, we perform a simulation to extract the NRMSE$_d$, the NRMSE between the estimated $\tilde{d}_J^\ell$ and the true d_J^ℓ, over a small range of magnetic field B_z, as shown in Fig.5(a). It is observed that NRMSE$_d$ decreases as Rabi frequency Ω_g increases near $B_z = 1$ μT. This explains why the NRMSE of waveform reconstruction with $\Omega_g/(2\pi) = 50$ MHz is the lowest among the four cases listed in Table 3.

Table 3 also indicates that the maximum detectable field range $B_{\text{Berry}}^{\max}$ increases and the sensitivity deteriorates as the Rabi frequency increases. Fig.5(b) shows the curves of probability readout difference $(P_{0\to1}^g - P_{0\to0}^g)$ versus B_z at four different Rabi frequencies, respectively. The maximum detectable field $B_{\text{Berry}}^{\max}$ is defined as the value of B_z when $(P_{0\to1}^g - P_{0\to0}^g)$ drops to the first minimum from the maximum at $B_z = 0$. A one-to-one correspondence exists between $(P_{0\to1}^g - P_{0\to0}^g)$ and B_z if $B_z < B_{\text{Berry}}^{\max}$.

Fig.5(b) indicates that $B_{\text{Berry}}^{\max}$ increases as the Rabi frequency increases. However, the change in probability difference is less sensitive to the change of B_z when B_z is close to zero, and the sensitivity deteriorates as Rabi frequency increases, consistent with the results listed in Table 3.

By considering the trade-off between sensitivity and maximum detectable field, we choose $\Omega_g/(2\pi) = 50$ MHz and reserve 5% of the ambient geomagnetic field to provide a ~ 1 μT offset when applying the Berry sequence.

The curve of $\Omega_g/(2\pi) = 50$ MHz in Fig.5(b) indicates that the maximum detectable magnetic field of a Berry sequence is $B_{\text{Berry}}^{\max} = 460.66$ μT, which is much higher than its counterpart of a Ramsey sequence, $B_{\text{Ramsey}}^{\max} = \pi/(\gamma_e T_s') = 1.12$ μT.

From Section IV-B, an NVE sample with spin-echo sensitivity of several tens of pT/$\sqrt{\text{Hz}}$ is not agile enough to accurately detect kHz geomagnetic fluctuations of sub-pT level immersed in spin-bath noise. Deliberately reserving a partial ambient geomagnetic field can provide a magnetic field offset to comply with the sensitivity limit.

For instance, the spin-echo sensitivity in (60) is 82.41 pT/$\sqrt{\text{Hz}}$, implying that the minimum detectable field is about 8.24 nT if a spin-echo sequence is applied to detect magnetic field at frequency of 10 kHz. If a Helmholtz coil is used to compensate for 99.9% of the ambient geomagnetic field B_{0z}, an offset of about 21 nT is added to $B_z(t)$ in (12), which is higher than the minimum detectable field of 8.24 nT for reconstructing VLF components in the waveform shown in Fig.1.

Similarly, the Berry sensitivity in (63) is 6.789 nT/$\sqrt{\text{Hz}}$, implying that the minimum detectable field is about 67.89 nT if a Berry sequence is applied to detect near-dc geomagnetic fluctuations of 100 Hz. If another Helmholtz coil is used to compensate for 95% of the ambient geomagnetic field, an offset of $\sim$ 1 μT is added to $B_z(t)$ in (50), which is higher than the minimum detectable field of 67.89 nT for reconstructing the near-dc components below 100 Hz in the waveform shown in Fig.1.

Supporting with the Helmholtz coils, the proposed NVE array and sensing protocols are capable of reconstructing the target waveform of geomagnetic fluctuations, which will be confirmed by simulations in the next Subsection.

D. WAVEFORM RECONSTRUCTION AND ERROR ANALYSIS

The performance of the proposed waveform reconstruction approach is evaluated with a noise power

$$\text{NP}(\tilde{B}_{f,N_{\text{NV}}}) = \int_0^{T_{\text{tot}}} \left|\tilde{B}_{f,N_{\text{NV}}}(t) - B_f(t)\right|^2 dt \quad (\text{T}^2) \tag{64}$$

defined over the total sensing time $T_{\text{tot}} = 4T_s$ as shown in Fig.1, with $T_s = 128$ μs, where $\tilde{B}_{f,N_{\text{NV}}}(t)$ is the waveform reconstructed with N_{NV} NV centers in each NVE.

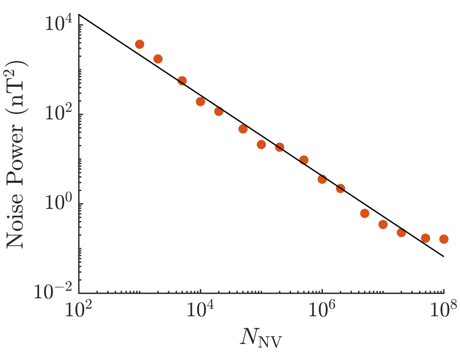

FIGURE 6. Noise power embedded in reconstructed geomagnetic waveform versus N_{NV}, ●: simulation data, ———: regression line on simulations data, NP$\propto N_{\text{NV}}^{-0.9}$.

Fig.6 shows that the noise power (NP) is related to the number of NV centers in each NVE as NP$\propto$ $N_{\text{NV}}^{-0.9}$, and the noise level is proportional to $N_{\text{NV}}^{-0.45}$. Thus, the signal-to-noise ratio (SNR) is proportional to $N_{\text{NV}}^{0.45}$, which falls within the standard quantum limit [30], [65].

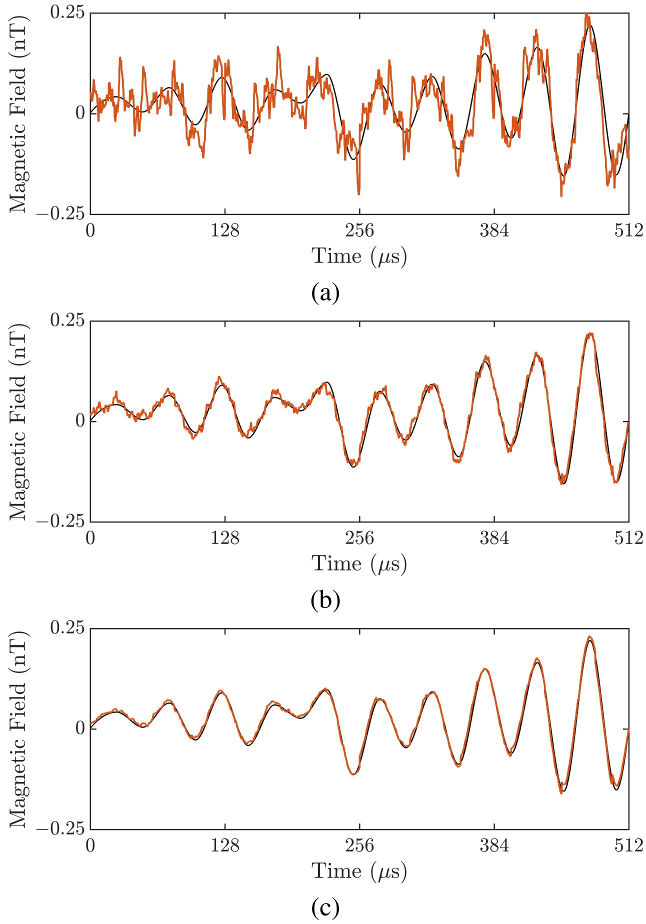

FIGURE 7. Reconstruction of geomagnetic fluctuations waveform in VLF band by using NVEs with different N_{NV}, ———: true waveform, ———: reconstructed waveform, (a) $N_{\text{NV}} = 10^6$, (b) $N_{\text{NV}} = 10^7$, and (c) $N_{\text{NV}} = 10^8$.

Fig.7 shows the reconstruction of geomagnetic fluctuations waveform in the VLF band by using NVEs with different N_{NV}. The reduction of noise power with larger N_{NV} effectively improves the accuracy of waveform reconstruction. Fig.7(a) shows the results with $N_{\text{NV}} = 10^6$. The shape of the geomagnetic waveform is discernible, but is severely perturbed by spin-bath noise.

Fig.7(b) shows that as the number of NV centers is increased to $N_{\text{NV}} = 10^7$, the perturbations on geomagnetic waveform are significantly mitigated. Fig.7(c) shows that with $N_{\text{NV}} = 10^8$, the geomagnetic fluctuations waveform is well reconstructed and almost overlaps with the true waveform in the black curve, suggesting that the proposed NVE array schematic and sensing protocols, accompanied with properly selected parameters, can effectively and accurately reconstruct a waveform of geomagnetic fluctuations in the VLF band.

V. HIGHLIGHTS, CONCLUSIONS AND PROSPECTS

A wavelet-based reconstruction approach is proposed to reconstruct a nonrepeatable waveform of geomagnetic fluctuations in the VLF band. Berry sequences and spin-echo sequences are combined for the first time to extract the scaling coefficients for reconstructing near-dc components and Haar wavelet coefficients for reconstructing high-frequency components, respectively.

We propose a novel schematic of utilizing an NVE array to implement the proposed wavelet-based sensing protocols for extracting these coefficients in one shot, followed by an inverse wavelet transform to reconstruct the waveform. Each NVE contains $N_{\rm NV} = 10^8$ NV centers and is controlled by an independent microwave drive. The signal averaging technique is adopted to simulate the readout of probability from $N_{\rm NV}$ NV centers.

A Berry sequence is applied on an NVE to extract the corresponding scaling coefficient via the accumulated geometric phase. The sensitivity is deteriorated to $\sim$ 6.8 nT/$\sqrt{\rm Hz}$ but the maximum detectable field is significantly extended over 460 μT, resolving the issues of dynamic phase ambiguity and hyperfine-induced detuning.

A worst-case sensitivity of $\sim$ 80 pT/$\sqrt{\rm Hz}$ is achieved when applying spin-echo sequences to extract wavelet coefficients of the seventh scale via the accumulated dynamic phase. We also propose the use of Helmholtz coils to partially compensate for the ambient geomagnetic field, enabling the NVE quantum sensors to comply with the limits of sensitivity and dynamic range.

The efficacy of the proposed sensing protocols is validated by reconstructing a waveform of geomagnetic fluctuations in the DEMETER satellite dataset. Possible factors that may affect the operation and performance of the proposed NVE array and sensing protocols have been analyzed and validated with simulations, including spin-bath noise, dynamic phase ambiguity, transverse magnetic field, residual ambient magnetic field, wavelet scales, Rabi frequency, sensitivity, maximum detectable magnetic field, and number of NV centers in each NVE.

NVE sensors are resilient to harsh environments and do not require frequent calibration. In the future, the proposed NVE array can be installed on nano-satellites to monitor global geomagnetic fluctuations, promoting studies in geophysics and space exploration. Moreover, quantum resources such as entanglement and squeezing can be harnessed to enhance the sensitivity of NVE quantum sensors.

ACKNOWLEDGMENT

The authors would like to acknowledge the DEMETER Scientific Mission Center and CDPP (Centre des Données de la Physique des Plasmas) for providing the magnetic field observation data in https://cdpp-archive.cnes.fr/.

REFERENCES

[1] C. L. Degen, F. Reinhard, and P. Cappellaro, “Quantum sensing, ” Rev. Mod. Phys., vol. 89, 035002, Jul. 2017.
[2] D. J. McCloskey et al., “Enhanced Widefield Quantum Sensing with Nitrogen-Vacancy Ensembles Using Diamond Nanopillar Arrays, ” ACS Appl. Mater. Interfaces, vol. 12, no. 11, pp. 13421-13427, Feb. 2020.
[3] C. Foy et al., “Wide-Field Magnetic Field and Temperature Imaging Using Nanoscale Quantum Sensors, ” ACS Appl. Mater. Interfaces, vol. 12, no. 23, pp. 26525-26533, Apr. 2020
[4] X. Wang et al., “Quantum diamond magnetometry for navigation in GNSS denied environments, ” arXiv:2302.06187 [math.OC], Feb. 2023.
[5] N. Aslam et al., “Quantum sensors for biomedical applications, ” Nat. Rev. Phys., vol. 5, pp. 157-169, Feb. 2023.
[6] F. Casola, T. van der Sar, and A. Yacoby, Probing Condensed Matter Physics with Magnetometry Based on Nitrogen-Vacancy Centres in Diamond, Nat. Rev. Materials, vol. 3, 17088, Jan. 2018.
[7] Q. Wang et al., “Hybrid NV Center Magnetometer with Directional Vector Resolution Based on Magnetic Flux Concentrators, ” IEEE Sensors J., vol. 23, no. 12, pp. 12719-12726, Jun. 2023.
[8] N. Olsen and C. Stolle, “Satellite Geomagnetism, ” Ann. Rev. Earth Planetary Sci., vol. 40, pp. 441-465, May 2012.
[9] J. H. Kim and H.-Y. Chang, “Geomagnetic Field Variations Observed by INTERMAGNET during 4 Total Solar Eclipses, ” J. Atmos. Solar-Terr. Phys., vol. 172, pp. 107-116, Jul. 2018.
[10] C. Constable, “Earth’s electromagnetic environment, ” Surveys Geophys., vol. 37, pp. 27-45, Dec. 2015.
[11] Z. Zhima et al., “Possible Ionospheric Electromagnetic Perturbations Induced by the Ms7.1 Yushu Earthquake, ” Earth, Moon, and Planets, vol. 108, pp. 231-241, May 2012.
[12] D. Budker and D. F. Jackson, Optical magnetometry. New York, NY, USA: Cambridge University Press, 2013.
[13] R. Kaltenbaek et al., “Quantum technologies in space,” Experimental Astronomy, vol. 51, no. 3, pp. 1677-1694, Jun. 2021.
[14] J. S. Bennett et al., “Precision magnetometers for aerospace applications: A review,” Sensors, vol. 21, no. 16, 5568, Jan. 2021.
[15] P. Alken, N. Olsen, and C. C. Finlay, “Co-estimation of geomagnetic field and in-orbit fluxgate magnetometer calibration parameters,” Earth, Planets and Space, vol. 72, no. 1, Apr. 2020.
[16] H. Luhr, N. Klocker, W. Oelschlagel, B. Hausler, and M. Acuna, “The IRM Fluxgate Magnetometer,” IEEE Trans. Geosci. Remote Sens., vol. GE-23, no. 3, pp. 259-261, May 1985.
[17] H. Korth et al., “Miniature atomic scalar magnetometer for space based on the rubidium isotope 87 Rb,” J. Geophys. Res. Space Phys., vol. 121, no. 8, pp. 7870-7880, Aug. 2016.
[18] F. Han, S. Harada, and I. Sasada, “Fluxgate and search coil hybrid: A low-noise wide-band magnetometer,” IEEE Trans. Magnetics, vol. 48, no. 11, pp. 3700-3703, Nov. 2012.
[19] M. Mandea, M. Holschneider, V. Lesur, and H. Lühr, “The Earth’s magnetic field at the CHAMP satellite epoch,” System Earth via Geodetic-Geophysical Space Techniques, Berlin, Germany: Springer, 2010.
[20] M. Parrot et al., “The Magnetic Field Experiment IMSC and Its Data Processing Onboard DEMETER: Scientific Objectives, Description and First Results, ” Planetary Space Sci., vol. 54, pp. 441-455, Apr. 2006.
[21] J. M. G. Merayo et al. “The Swarm Magnetometry Package, ” in Small Satellites for Earth Observation: Selected Contributions. Springer, 2008.
[22] CDPP Archive. [Online]. Available: http://cdpp-archive.cnes.fr/. Accessed on: Jul. 13, 2023.
[23] Y.-Y. Ho, H.-K. Jhuang, Y. Z. Su, and J. B. Liu, “Seismo-ionospheric anomalies in total electron content of the GIM and electron density of DEMETER before the 27 February 2010 M8.8 Chile earthquake, ” Advances in Space Res., vol. 51, pp. 2309-2315, Jun. 2013.
[24] K. Ryu et al., “Suspected Seismo-Ionospheric Coupling Observed by Satellite Measurements and GPS TEC Related to the M 7.9 Wenchuan Earthquake of 12 May 2008, ” J. Geophys. Res.: Space Phys., vol. 119, no. 12, pp. 10305-10323, Dec. 2014.
[25] M. Parrot, A. L. Buzzi, O. Santolik, J.-J. Berthelier, J. A. Sauvaud, and J.-P. Lebreton, “New observations of electromagnetic harmonic ELF emissions in the ionosphere by the DEMETER satellite during large magnetic storms, ” J. Geophys. Res.: Space Phys., vol. 111, A08301, Jan. 2006.
[26] Z. Zhima et al., “Storm Time Evolution of ELF/VLF Waves Observed by DEMETER Satellite, Journal of Geophysical Research: Space Physics, ” J. Geophys. Res.: Space Phys., vol. 119, pp. 2612-2622, Apr. 2014.
[27] M. Schmelz and R. Stolz, “Superconducting quantum interference device (SQUID) magnetometers,” High Sensitivity Magnetometers; A. Grosz, M. J. Haji-Sheikh, S. C. Mukhopadhyay Eds.; Springer International Publishing: Cham, Switzerland, 2017.

[28] H. Hao, H. Wang, L. Q. Chen, J. Wu, L. Qiu, and L. Rong, "Initial results from SQUID sensor: Analysis and modeling for the ELF/VLF atmospheric noise," Sensors, vol. 17, no. 2, 371, Feb. 2017.

[29] F. M. Stürner et al., "Integrated and portable magnetometer based on nitrogen-vacancy ensembles in diamond," Adv. Quantum Tech., vol. 4, no. 4, 2000111, Feb. 2021.

[30] J. F. Barry et al., "Sensitivity Optimization for NV-Diamond Magnetometry, " Rev. Mod. Phys., vol. 92, 015004, Mar. 2020.

[31] E. Janitz, K. Herb, L. A. Völker, W. S. Huxter, C. L. Degen, and J. M. Abendroth, "Diamond surface engineering for molecular sensing with nitrogen-vacancy centers," J. Mater. Chem. C, vol. 10, 13533, Sep. 2022.

[32] T. Wolf et al., "Subpicotesla Diamond Magnetometry, " Phys. Rev. X, vol. 5, 041001, Oct. 2015.

[33] I. Fescenko et al., "Diamond magnetometer enhanced by ferrite flux concentrators," Phys. Rev. Research, vol. 2, no. 2, 023394, Jun. 2020.

[34] A. Strangfeld, O. Carraz, A. Eiden, A. Hélière, and P. Silvestrin, "Quantum sensing for earth observation at the European Space Agency: latest developments, challenges, and future prospects, " Proc. SPIE 12729, Sensors, Systems, and Next-Generation Satellites XXVII, 127290B, Oct. 2023.

[35] W. Kozlowski and S. Wehner, "Towards Large-Scale Quantum Networks, " in NANOCOM '19: Proceedings of the Sixth Annual ACM International Conference on Nanoscale Computing and Communication, Sep. 2019, p. 3.

[36] E. Pelucchi et al., "The Potential and Global Outlook of Integrated Photonics for Quantum Technologies, " Nat. Rev. Phys., vol. 4, pp. 194-208, Mar. 2022.

[37] Y. Hatano et al., "Simultaneous thermometry and magnetometry using a fiber-coupled quantum diamond sensor, " Appl. Phys. Lett. vol. 118, 034001, Jan. 2021.

[38] X. Wang et al., "Portable diamond NV magnetometer head integrated with 520 nm diode laser," IEEE Sensors J., vol. 22, no. 6, pp. 5580-5587, Mar. 2022.

[39] J. Zopes and C. L. Degen, "Reconstruction-free quantum sensing of arbitrary waveforms, " Phys. Rev. Appl., vol. 12, 054028, Nov. 2019.

[40] A. Cooper, E. Magesan, H. N. Yum, and P. Cappellaro, Time-Resolved Magnetic Sensing with Electronic Spins in Diamond, Nat. Commun., vol. 5, 3141, Jan. 2014.

[41] C.-W. Kiang, J.-J. Ding, and J.-F. Kiang "Quantum sensing of fast time-varying magnetic field with Daubechies wavelets," IEEE Access, vol. 12, pp. 23181-23189, Feb. 2024.

[42] N. Xu et al., "Wavelet-Based Fast Time-Resolved Magnetic Sensing with Electronic Spins in Diamond, " Phys. Rev. B, vol. 93, 161117, Apr. 2016.

[43] G. Strang, "Wavelet Transforms versus Fourier Transforms, " Bulletin of the American Mathematical Society, vol. 28, pp. 288-306, Apr. 1993.

[44] S. Mallat, A Wavelet Tour of Signal Processing: The Sparse Way, 3rd Ed. Academic Press, 2009.

[45] N. Bar-Gill et al., "Suppression of Spin-Bath Dynamics for Improved Coherence of Multi-Spin-Qubit Systems, Nature Communications, " Nat. Commun., vol. 3, 858, Jan. 2012.

[46] S. Lin et al., "Temperature-Dependent Coherence Properties of NV Ensemble in Diamond up to 600 K, " Phys. Rev. B, vol. 104, 155430, Oct. 2021.

[47] D. Le Sage et al., "Efficient photon detection from color centers in a diamond optical waveguide," Phys. Rev. B, vol. 85, no. 12, 121202(R), Mar. 2012.

[48] S. Felton et al., "Hyperfine interaction in the ground state of the negatively charged nitrogen vacancy center in diamond," Phys. Rev. B, vol. 79, no. 7, Feb. 2009.

[49] Y. Yang et al., "Observing hyperfine interactions of NV− centers in diamond in an advanced quantum teaching lab," Am. J. Phys., vol. 90, no. 7, pp. 550-560, Jul. 2022.

[50] Z.-H. Wang and S. Takahashi, "Spin decoherence and electron spin bath noise of a nitrogen-vacancy center in diamond, " Phys. Rev. B, vol. 87, 115122, Mar. 2013.

[51] Y. Chou, S.-Y. Huang, and H.-S. Goan, "Optimal control of fast and high-fidelity quantum gates with electron and nuclear spins of a nitrogen-vacancy center in diamond, " Phys. Rev. A, vol. 91, 052315, May 2015.

[52] M. Joos, D. Bluvstein, Y. Lyu, D. Weld, and A. Jayich, "Protecting qubit coherence by spectrally engineered driving of the spin environment, " npj Quantum Inf., vol. 8, 47, Apr. 2022.

[53] A. Nits et al., "gwastro/pycbc: v2.2.1 release of PyCBC, " doi: 10.5281/zenodo.8190155, Jul. 2023.

[54] E. Bibbona, G. Panfilo, and P. Tavella, "The Ornstein-Uhlenbeck Process as a Model of a Low Pass Filtered White Noise, " Metrologia, vol. 45, pp. S117-S126, Dec. 2008.

[55] H. Park, J. Lee, S. Han, S. Oh, and H. Seo, "Decoherence of nitrogen-vacancy spin ensembles in a nitrogen electron-nuclear spin bath in diamond," npj Quantum Inf., vol. 8, no. 1, Aug. 2022.

[56] P. Rembold, N. Oshnik, M. M. Muller, S. Montangero, T. Calarco, and E. Neu, "Introduction to quantum optimal control for quantum sensing with nitrogen-vacancy centers in diamond," AVS Quantum Sci., vol. 2, 024701, Jun. 2020.

[57] T. Lenz, A. Wickenbrock, F. Jelezko, G. Balasubramanian, and D. Budker, "Magnetic sensing at zero field with a single nitrogen-vacancy center," Quantum Sci. Technol., vol. 6, no. 3, 034006, Jun. 2021.

[58] H. Clevenson, E. H. Chen, F. Dolde, C. Teale, D. Englund, and D. Braje, "Diamond-nitrogen-vacancy electronic and nuclear spin-state anticrossings under weak transverse magnetic fields," Phys. Rev. A, vol. 94, no. 2, Aug. 2016.

[59] M. Auzinsh et al., "Hyperfine level structure in nitrogen-vacancy centers near the ground-state level anticrossing," Phys. Rev. B, vol. 100, no. 7, Aug. 2019.

[60] K. Arai, J. Lee, C. Belthangady, D. R. Glenn, H. Zhang, and R. L. Walsworth, "Geometric phase magnetometry using a solid-state spin," Nat. Commun., vol. 9, no. 1, 4996, Nov. 2018.

[61] P. J. Leek et al., "Observation of Berry's phase in a solid-state qubit," Science, vol. 318, no. 5858, pp. 1889-1892, Dec. 2007.

[62] N. M. Nusran and G. Dutt, "Optimizing phase-estimation algorithms for diamond spin magnetometry," Phys. Rev. B, vol. 90, no. 2, 024422, Jul. 2014.

[63] Y. Li et al., "Noise suppression of nitrogen-vacancy magnetometer in lock-in detection method by using common mode rejection," Micromachines, vol. 14, no. 10, 1823, Sep. 2023.

[64] E. Bauch et al., "Decoherence of ensembles of nitrogen-vacancy centers in diamond, " Phys. Rev. B, vol. 102, 134210, Oct. 2020.

[65] I. Schwartz et al., "Blueprint for nanoscale NMR," Scientific Reports, vol. 9, 6938, May 2019.

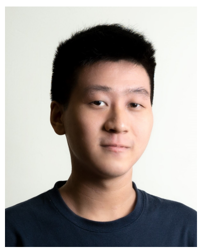

CHOU-WEI KIANG received his B.S. degree in electrical engineering from National Taiwan University, Taipei, Taiwan, in 2022. He is currently a research assistant at National Taiwan University. His research interests include quantum sensing and engineering, quantum information processing, optics and electromagnetics, remote sensing, and signal processing applications.

JEAN-FU KIANG (Life Senior, IEEE) received his Ph.D. degree in electrical engineering from the Massachusetts Institute of Technology, Cambridge, MA, USA, in 1989.

Since 1999, he has been a Professor with the Department of Electrical Engineering and Graduate Institute of Communication Engineering, National Taiwan University. His research interest is to explore different ideas, theories and methods on various electromagnetic phenomena and possible applications, including remote sensing, radar signal processing, antennas, phased arrays, propagation, scattering, communications, and so on. Some of his works can be viewed in his website: http://cc.ee.ntu.edu.tw/∼jfkiang/selected_publications.html